Environmental Science Nano

Visualization of Label-Free Titanium Dioxide Nanoparticles Deposition on Surfaces with Nanoscale Roughness

Journal:	*Environmental Science: Nano*
Manuscript ID	EN-ART-09-2018-000984.R2
Article Type:	Paper
Date Submitted by the Author:	27-Nov-2018

Complete List of Authors:	Kananizadeh, Negin; University of Nebraska-Lincoln College of Engineering, Civil Engineering Peev, Darin; University of Nebraska-Lincoln College of Engineering, Electrical and Computer Engineering Delon, Thompson; University of Nebraska-Lincoln College of Engineering, Civil Engineering Schubert, Eva; University of Nebraska-Lincoln Bartelt-Hunt, Shannon; University of Nebraska-Lincoln College of Engineering, Civil Engineering Schubert, Mathias; University of Nebraska-Lincoln Zhang, Jianmin; Sichuan University Li, Yusong; University of Nebraska-Lincloln, Civil Engineering

Environmental Significance Statement:

Understanding the transport of engineered nanoparticles (ENPs) and their interaction with environmental surfaces is critical to predicting their fate and environmental implications. Titanium dioxide nanoparticles (TiO2NPs) are one of the most widely used ENPs in the commercial industry, which was detected in the environment. Based on the principles of generalized ellipsometry (GE), we demonstrated an innovative, label-free method to visualize and quantify the deposition and transport of TiO2NPs on engineered surfaces with nanoscale roughness, i.e., slanted columnar thin film (SCTF) surfaces.

Visualization of Label-Free Titanium Dioxide Nanoparticles Deposition on Surfaces with Nanoscale Roughness

Negin Kananizadeh[1,2], Darin Peev[2,3], Thompson Delon[1,2], Eva Schubert[2,3], Shannon Bartelt-Hunt[1,2], Mathias Schubert[2,3,5,6*], Jianming Zhang[7], and Yusong Li[1,2*]

[1]Department of Civil Engineering, University of Nebraska-Lincoln, Lincoln, NE 68588, United Stated

[2]Center for Nanohybrid Functional Materials, University of Nebraska-Lincoln, Lincoln, NE 68588, United States

[3] Department of Electrical and Computer Engineering, University of Nebraska-Lincoln, Lincoln, NE 68588, United States

[5]Department of Physics, Chemistry, and Biology (IFM), Linkoping University, Linkoping, 58183, Sweden

[6]Leibniz Institute of Polymer Research (IPF) Dresden, Dresden, D 01005, Germany

[7]State Key Laboratory of Hydraulics and Mountain River Engineering, Sichuan University, Chengdu, 610065, China

Submitted to

Environmental Science: Nano

*Corresponding authors: Email: yli7@unl.edu, Email: schubert@engr.unl.edu

Abstract

Understanding the transport of engineered nanoparticles (ENPs) and their interaction with environmental surfaces is critical to predicting their fate and environmental implications. Here, we report an innovative technique to visualize and quantify the deposition of titanium dioxide nanoparticles (TiO_2NP) on engineered surfaces with nanoscale roughness, i.e., slanted columnar thin films (SCTFs). The attachment of TiO_2NP on the surface of SCTFs changed the optical property of SCTFs, which was detected using a generalized ellipsometry (GE)-based instrument, an anisotropy contrast optical microscope (ACOM). An anisotropic effective medium model was applied to quantitatively analyze ACOM images of SCTF surfaces, which provided the mass distribution of TiO_2NP. The TiO_2NP mass measured by ACOM was in good agreement with the known amount of TiO_2NP mass dispersed by controlled piezoelectric plotting. The detection of a few picograms of nanoparticle mass by an individual pixel measuring 7×7-micrometer squared was demonstrated. Further, a glass microfluidic channel with SCTF embedded was developed. The areal mass density of attached TiO_2NP on SCTF surfaces as they flow through the channel under various flow rates was quantitatively measured in situ. At the end of the experiment, the distribution of the attached TiO_2NP on the SCTF surface was visualized. The averaged mass density estimated by integrating the distribution map was in close agreement with the estimation from dynamic measurements and between repeating experiments. The capability of this novel technique to sense, quantify and visualize the mass distribution of TiO_2NP provides a valuable approach to investigate the behavior of nanoparticles at the interface of flow and rough surfaces.

Keywords: Anisotropy Contrast Optical Microscopy, Ellipsometry, Anisotropic Bruggeman Effective Medium Approximation, Nano-plotting, Microfluidic Channel, Titanium Dioxide Nanoparticles, Rough Surface

1. Introduction

Engineered nanoparticles (ENPs) are widely used in many commercial products, which can lead to their release into the environment during use or after disposal. The production of titanium dioxide nanoparticles (TiO_2NPs), one of the most widely used ENPs in commercial industry, was estimated to be 2.4 million tons in the US by 2025, and 3 to 30 percent of that may end up in water bodies[1,2]. Recent work has found that the toxicity of TiO_2NP can be increased by over an order of magnitude when they are exposed to ultraviolet light, a typical case in clear water[3]. Understanding the transport of ENPs and their interaction with environmental surfaces is critical to predicting their fate and environmental implications.

The majority of ENP transport studies have been conducted using a cylindrical column packed with environmental media, i.e., silica sands, glass beads, or soils[3–10]. By measuring the concentration change of ENPs at the inlet and outlet of the column, deposition of ENP in the environmental media can be estimated using a classical filtration theory or a modified version of the theory. Although column experiments present a relatively realistic setup to environmental porous media, the interaction between ENPs and surfaces cannot be directly measured. In addition to traditional column experiments, the deposition of ENPs onto solid surfaces has been recently measured using quartz crystal microbalance with dissipation (QCM-D)[11–13]. Although QCM-D can measure the direct interaction between ENPs and a surface, most studies used very flat silica or metal oxide surfaces to mimic natural soil and sediment surfaces, which could be an oversimplification by totally neglecting the influence of surface roughness. Recently, a model rough surface[12] was incorporated onto QCM-D surfaces to investigate the impact of surface roughness on TiO_2NP deposition. This approach provides a method to directly measure the interaction of TiO_2NP and a model rough surface; however, QCM-D lacks visualization of the attached ENPs on the surfaces.

To better evaluate and visualize ENPs deposition, microfluidic channels, in conjunction with various visualization techniques, were developed[14–19]. For example, an innovative micromodel system with well-arranged 2-D cylindrical collectors was used to visualize ENP deposition and quantify the single collector efficiency factor[19]. Such systems, however, rely on

the fluorescent labeling of ENPs for visualization. The use of fluorescent labels may modify the properties of a given ENP, for example TiO_2NP, or may interfere with the interaction between TiO_2NPs and surfaces. Therefore, it is often desirable to obtain optical images without applying fluorescent labels. Previously, Guzman et al. used a 2-D micromodel of porous media to investigate the effect of pH on TiO_2NPs aggregation and transport in porous media[14]. The concentration of TiO_2NP at the effluent of the 2-D micromodel was measured using UV-VIS, and a CCD camera was used to visualize the pore clogging. Here, the distribution of particle aggregates was only visualized qualitatively.

In this work, we present the application of an innovative label-free imaging technique sensitive to nanoscopic objects - Anisotropy Contrast Optical Microscopy (ACOM)[20] - to obtain images and quantify the mass distribution of TiO_2NP attached to engineered porous, optically anisotropic, slanted columnar thin films (SCTFs). ACOM uses principles of generalized ellipsometry (GE), a highly accurate, non-destructive, and non-invasive optical method[21,22], which measures the change in polarization when light reflects off or transmits through a sample[20,23–28]. Here, SCTFs served as an anisotropic substrate for GE measurements, as well as a surface with a controlled roughness height. For the first step of our investigation, the change in the anisotropic optical response of SCTFs due to local deposition of TiO_2NP drops with known mass on the surface of SCTF was imaged and measured using ACOM statically in the air ambient. We then used this technique to measure and visualize the deposition of TiO_2NP onto SCTF surfaces inside a microfluidic channel dynamically under flow conditions. Here, an innovative approach to embed SCTF in a glass microfluidic channel was developed, which is not invasive to the SCTF thin films.

2. Materials and Methods

2.1. Nanoparticle Preparation and Characterization

Titanium dioxide nanoparticles (TiO_2NPs) stabilized by polyacrylate sodium were purchased from Sciventions Company (Toronto, Canada). Different concentrations of TiO_2NPs (50, 750, and 1500 ppm) were prepared in Nanopure water (18.2 MΩ-cm, Barnstead Nano-pure Systems, Thermo Scientific Inc., Waltham, MA) and sonicated for at least one hour (FS 60, 100W, 42 kHz, Fisher Scientific, Pittsburg, PA). The pH of the solution was then adjusted to 7 ± 0.1 using 100 mM NaOH or HCl. The number-weighted hydrodynamic diameter distribution of the solution

was measured using a 90 Plus Particle Size Analyzer. The particle zeta potential was then measured using a ZetaPALS Zeta Potential Analyzer (Brookhaven Instruments Corporation, Holtsville, NY).

2.2. SCTF Preparation

500 nm-thick SCTF made of silicon (Si-SCTF) was deposited on a glass surface in a highly vacuum chamber using a glancing angle deposition (GLAD)[29] technique. The prepared Si-SCTF samples were then covered by a 4-nm-thick conformal alumina (Al_2O_3-Si-SCTF) using atomic layer deposition (ALD) technique (Fiji 200, Cambridge Nanotech). Al_2O_3 was used to coat a Si-SCTF surface (Al_2O_3-Si-SCTF) to mimic metal oxides on sand surfaces, which are known to greatly contribute to nanoparticle deposition[23,30,31]. Scanning electron microscopy (SEM) was then performed on the Al_2O_3-Si-SCTF surface using FEI Nova NanoSEM450 field emission SEM. Detailed experimental methods are in the supporting information.

To measure TiO_2NP on the SCTF surface in air ambient, patterns measuring approximately 1×1 mm^2 in the shape of an 'N' that were filled with Al_2O_3-Si-SCTF were prepared to create an anisotropy surface. Detailed experimental methods are in the supporting information.

2.3. Microfluidic Chip Fabrication

In this work, we developed an innovative non-destructive method to fabricate glass microfluidic chips with SCTFs embedded on top using a two-step process. First, a spacing mold that defines the channel height and its pattern on the bottom glass slide was developed using a photolithography technique (Figure 1). Second, the spacing mold and the top glass slide were bonded using a UV curing glue.

To make the spacing mold, Omni coat (MicroChem Co., Westborough, MA) was first spin-coated onto a circular glass substrate (with a 31.75 mm diameter and 1.5 mm thickness) at 3000 rpm for 30 sec. This process can improve adhesion between the glass substrate and SU8-5 photoresist, which is needed in the next step. The sample was then baked at 200°C for 1 min. To achieve a thickness of 14 μm, SU8-5 (MicroChem Co., Westborough, MA) was then spin-coated at 1300 rpm for 30 sec on the glass substrate covered with Omni coat, then soft-baked for 2 min

at 65°C followed by 5 min at 95°C. The glass substrate with a SU8-5 cover was then exposed to UV for 13 sec using an exposure tool. Following exposure, a post-bake of 1 min at 65°C and 2 min at 95°C were performed to cross-link the exposed area of the film. Finally, the designed structure was developed in the SU-8 developer for 3 min. The final mold product was then rinsed with isopropyl alcohol (IPA) and dried with nitrogen.

In the second step, the spacing mold was bonded with a glass slide, which has two holes drilled and Al_2O_3-Si-SCTF grown as discussed in the SCTF preparation section. NOA-89 UV curing glue (Norland Products, Inc. Cranbury, NJ) was nano-plotted between the pore space of SU8-5 using a GeSiM 2.1 nano-plotter (GeSiM Co., Germany). To bring the viscosity of NOA-89 down, a heatable nano-tip manufactured by GeSiM was used at a temperature of 50°C. To avoid NOA-89 in contact with water in the tubes and the tip of the nano-plotter, 2 µl ethyl methyl ketone and 20 µl of cyclohexanone (Sigma-Aldrich Co., St. Louis, MO) with 15 µl of an air gap in between were aspirated inside the heatable nano-tip. The buffer solutions and the NOA-89 were stored in a cooled microplate at 12°C to reduce their rate of evaporation. NOA-89 was plotted on 1315 spots along the center line of the pore space with two drops at each location and a distance of 80 µm maintained between two adjacent locations, which ensures that a sufficient amount of glue filled in the space between the SU8-5 molds. Following plotting, the top glass slide with the Al_2O_3-Si-SCTF was then aligned and pressed on top of the spacing mold, which was then put under UV light for 20 minutes to allow the two parts to bond by NOA89. Note that to achieve the highest intensity change using ACOM, the experimental slanting direction (Figure 1) of the Al_2O_3-Si-SCTF sample was set to 45° with respect to the flow direction.

Prior to the experiment, the microfluidic channel was oxygen-plasma cleaned inside the ALD chamber at 70°C to remove any remaining residual NOA-89 evaporated on the surface of the Al_2O_3-Si-SCTF. The inlet and outlet ports of the cleaned and prepared channel were then sealed using Tygon tubes (ID=0.02'', OD=0.06'') (eMurdock Co.).

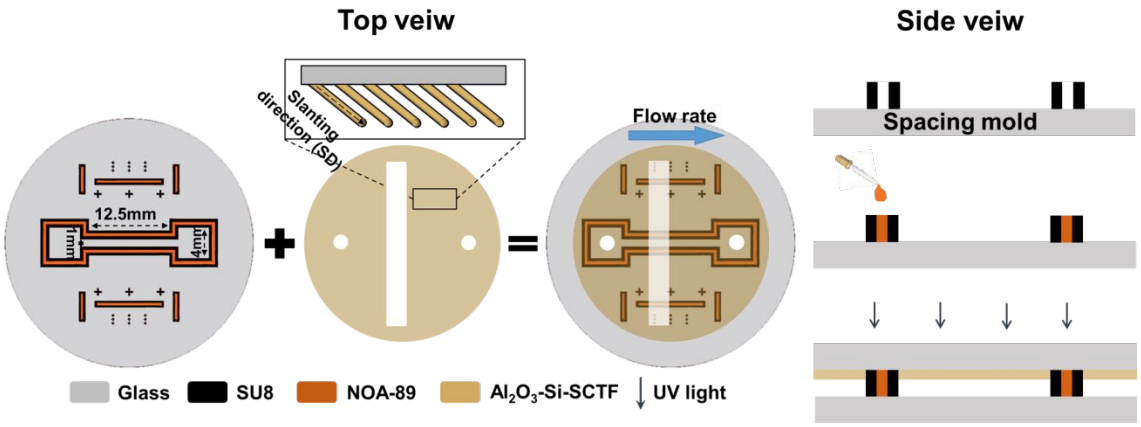

Fig. 1 Schematic of glass microfluidic chip fabrication with embedded Al_2O_3-Si-SCTF using photo lithography, glancing angle deposition technique (GLAD), atomic layer deposition technique (ALD), and nano-plotting.

2.4. ACOM Measurement and GE Analysis

ACOM can detect ultra-small amounts of organic as well as inorganic particulates with nanoscopic dimensions based on the optical contrast of an anisotropic filter. Figure 2a shows a sketch of the ACOM setup. A 100 W short arc Mercury lamp provides the light source (S). The light passes through a monochromator (M), a rotating Glan-Thompson polarizer (P), and then the anisotropic and semi-transparent sample of Al_2O_3-Si-SCTF on glass substrate. In this study, the wavelength of the light was set to 633 nm. An infinity corrected microscope objective (MO) collects light from the sample, which then passes a rotating compensator (C) and another fixed Glan-Thompson polarizer acting as analyzer (A). Finally, a low-noise Photometrics Evolve 512 Delta CCD camera gathers the intensity pictures. Detailed information of the instrument, its calibration and operation can be found in our previous publication[20]. In ACOM, the polarizer azimuth (α_p) was set to rotate 1° at each step while the compensator azimuth setting was rotating three times faster ($\alpha_c=3\alpha_p$). A total of 360 different intensity images (Figure 3b), each having 512 by 512 pixel points, were then captured by the CCD camera during the rotation scan. The volumetric fraction of the deposited TiO_2NP (f_{TiO_2}) on the SCTF layer for each pixel of the intensity image was obtained by best-matching model calculations of the intensity data (I_D) using an optical ellipsometry-based anisotropic Bruggeman effective medium approximation (AB-EMA) model[32], as briefly described below.

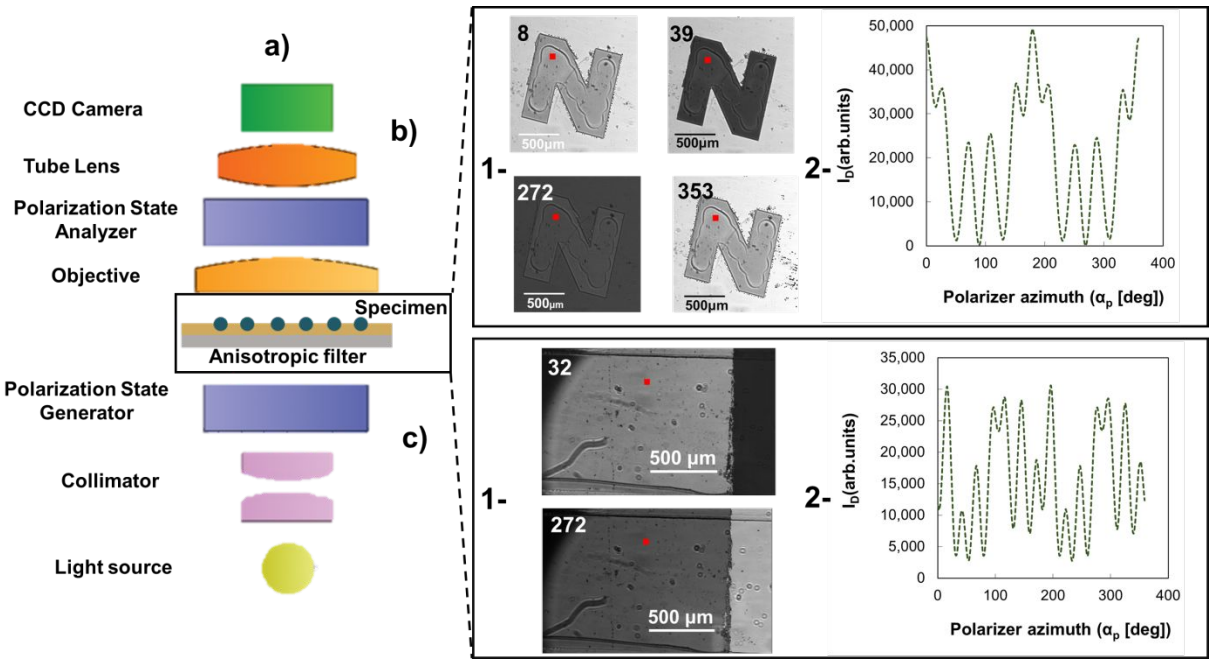

Fig. 2 Schematic of the a) anisotropic contrast optical microscope (ACOM). The polarization state generator consists here of a linear polarizer, the polarization state analyzer consists of a half-wave plate and a linear polarizer[20]. b-1) ACOM intensity images at selected polarizer azimuth (α_p) of 8°, 39°, 272°, and 353° of Al_2O_3-Si-SCTF inside an `N'-shape area for sample `Test 1-3' with piezo-electrically printed nano-liter-sized volumes of nanoparticle solution and b-2) a single-pixel ACOM intensity data (I_D) for 360 polarizer azimuth positions of α_p. c-1) ACOM intensity images at selected polarizer azimuth (α_p) of 32°, 272° of Al_2O_3-Si-SCTF inside a microfluidic channel `Test 2-3' with TiO_2NP deposited on it and b-2) a single-pixel ACOM intensity data (I_D) for 360 polarizer azimuth positions of α_p. The specimen (TiO_2NPs) attachment on anisotropic filter can be measured using ACOM. The hypothetical pixel positions are indicated in the ACOM images by a red square, which is drawn approximately 10 times larger than the pixel size. For further details of the ACOM instrument see peev et al.[20].

The AB-EMA models of the Al_2O_3-Si-SCTF in the air ambient and Al_2O_3-Si-SCTF in the microfluidic channel (water ambient) are represented in Figure 3. In the air ambient, two stratified optical layers, i.e., an anisotropic model layer (AB-EMA) representing the Si-SCTF layer on top of an isotropic glass (substrate) model layer with the refractive index of BK7 (Figure 4a)[33], were considered. In the microfluidic channel (Figure 4b), four stratified layers, i.e., an isotropic glass layer (optical constants of BK7), an AB-EMA layer of the anisotropic Al_2O_3-Si-SCTF, an isotropic 14 µm layer of water (water optical properties), and another isotropic glass layer (optical constants of BK7), were included. The optical effect of the 4-nm conformal alumina layer was included by finding effective optical constants for the alumina-coated Si columns prior to the TiO_2NP deposition experiment[23]. The structural and optical properties of Al_2O_3-Si-SCTF using the

ABM-EMA layer was described by parameters including SCTF thickness (H), slanting angle (Θ), slating plane azimuth relative to the linear polarization direction of the fixed analyzer azimuth (Φ), non-spherical depolarization parameters (q_z, and $split_{xy}$), and the volumetric fraction of constituents (f_{Si}, $f_{ambinet}$)[23,28,34]. Here, depolarization factors (q_z, q_x, q_y) along the z, x, and y major optical polarizability axes of the SCTF are representative for the relative dimensions of equivalent elliptical inclusions[32,35]. The anisotropic optical properties of the Al_2O_3-Si-SCTF model layer are then described by three dielectric functions, which correspond to the three major optical polarizability axes. Considering m constituent materials, the AB-EMA equation is as follow:

$$\sum_{n=1}^{m} \%n \frac{(\varepsilon_n - \varepsilon_{effj})}{\varepsilon_{effj} + q_{n,j}(\varepsilon_n - \varepsilon_{effj})} = 0, \quad (1\text{-}1)$$

$$\sum_{n=1}^{m} \%n = 1, \quad (1\text{-}2)$$

$$\mathcal{E} = N^2 = (\eta + ik)^2, \quad (1\text{-}3)$$

$$q_x = (1 - qz) \times split_{xy}, \quad (2\text{-}1)$$

$$q_x + q_y + q_z = 1, \quad (2\text{-}2)$$

Here, %n is the volume fraction of the n^{th} constituent material, ε_{effj} is the effective dielectric function along axis j, j = x,y,z, ε_n is the bulk dielectric function of the n^{th} constituent material, η is the index of refraction, κ is the extinction coefficient, and N is the complex index of refraction[24,36]. Prior to TiO_2NP exposure, the AB-EMA model approach was performed by best matching all single-pixel data sets of I_D, independently for each pixel point, using the software package WVASE32™ (J.A. Woollam Co., Inc., Lincoln, NE). The 360 I_D data for each pixel point measured by ACOM was compared to the 360 I_D calculated from the AB-EMA model until the best match between the measured and calculated I_D was achieved. The defined optical model interprets the properties of Al_2O_3-Si-SCTF (H, Θ, Φ, q_z, $split_{xy}$, f_{Si}, $f_{ambient}$) which is the averaged best-matched parameters of all pixel points. Then, after surface exposure to TiO_2NP, the volume fraction of TiO_2NPs (f_{TiO_2}) was added to the AB-EMA layer as the only best-matching parameters such that (f_{Si} + $f_{ambinet}$ + f_{TiO_2}= 100% to find the areal mass density of attached TiO_2NPs (Γ_{TiO_2}) on the Al_2O_3-Si-SCTF surface for each pixel point:

$$\Gamma_{TiO_2} = f_{TiO_2} \times H \times \rho_{TiO_2} \quad (3)$$

Here, ρ_{TiO_2} is the density of TiO_2NPs (3.9 g/ml)[20].

When TiO_2NP attach on the surface of Al_2O_3-Si-SCTF, whether on top or deep down on SCTF posts, ACOM detects the change in the optical properties of the posts, and proper AB-EMA model quantifies the overall deposited TiO_2NP on Al_2O_3-Si-SCTF surface. AB-EMA model is based on a homogenization concept. It assumes a well-mixed SCTF, water and attached particle system for each individual pixel point. Based on the homogenization concept, and the fact that the Al_2O_3-Si-SCTF are semi-transparent to the incoming polarized light, this technique can identify the amount of TiO_2NP attachment at a single pixel point on the X-Y plane of Al_2O_3-Si-SCTF, including both TiO_2NP deposited deep inside the spaces between the posts and those deposited closer to the surface of SCTF.

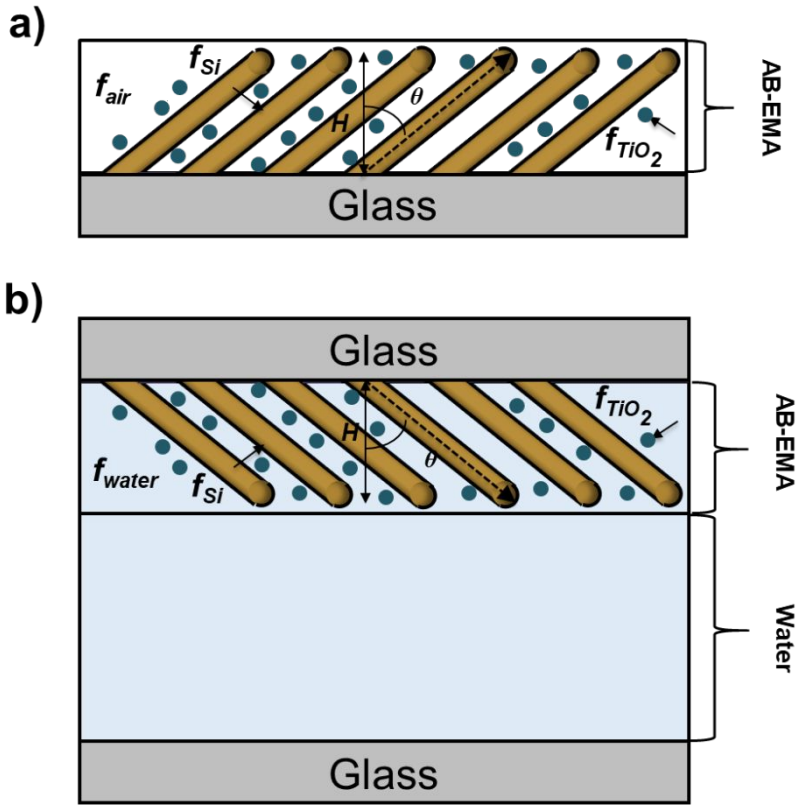

Fig. 3 Schematic of the AB-EMA ellipsometry model for Al_2O_3-Si-SCTF on a) glass substrate in air ambient with TiO_2NP attached on its surface and b) inside microfluidic channel in water ambient with TiO_2NP attached on its surface used in the analysis of the ACOM images.

2.5. Sensing Experiments in Air Ambient

Three `N'-shape samples (Figure 4) were prepared to detect $TiO_2$NP in air ambient (Test 1-1, Test 1-2, Test 1-3). For Test 1-1 and Test 1-2, respectively, 12 locations along the center line of the `N'-shape Al_2O_3-Si-SCTF were printed with sonicated 750 ppm and 1500 ppm TiO_2NP solutions twice, that is, every location on the center line received 2 drops, where the distance between each drop location along the center line was maintained to be 125 μm. For Tests 1-3, four drops of 1500 ppm TiO_2NP solution were printed at each location. A stroboscope camera image analysis was performed within the nano-plotter instrumentation, and the average volumes of the drops were determined as 0.65 nL, 0.66 nL, and 1 nL for Test 1-1, Test 1-2, and Test 1-3, respectively. The total mass of TiO_2NP printed thereby for Test 1-1, Test 1-2, and Test 1-3 were estimated as 12 ng, 24 ng, and 72 ng, respectively, based on the total printed volumes and the TiO_2NP solution concentrations. After the piezoelectric printing step, the sample was left to dry for 30 minutes before taking intensity images using the ACOM instrument.

Properties of the Al_2O_3-Si-SCTF, including thickness (H), slanting angle (Θ), slanting plane azimuth relative to the linear polarization direction of the fixed analyzer azimuth (Φ), fraction of constituents (f_{Si}, f_{air}), depolarization factors (q_z, $split_{xy}$), and plotted TiO_2NP on Al_2O_3-Si-SCTF surface (f_{TiO_2}), were estimated by best matching the ACOM recorded intensity data using a proper GE model, as explained above in the ACOM measurement GE analysis section.

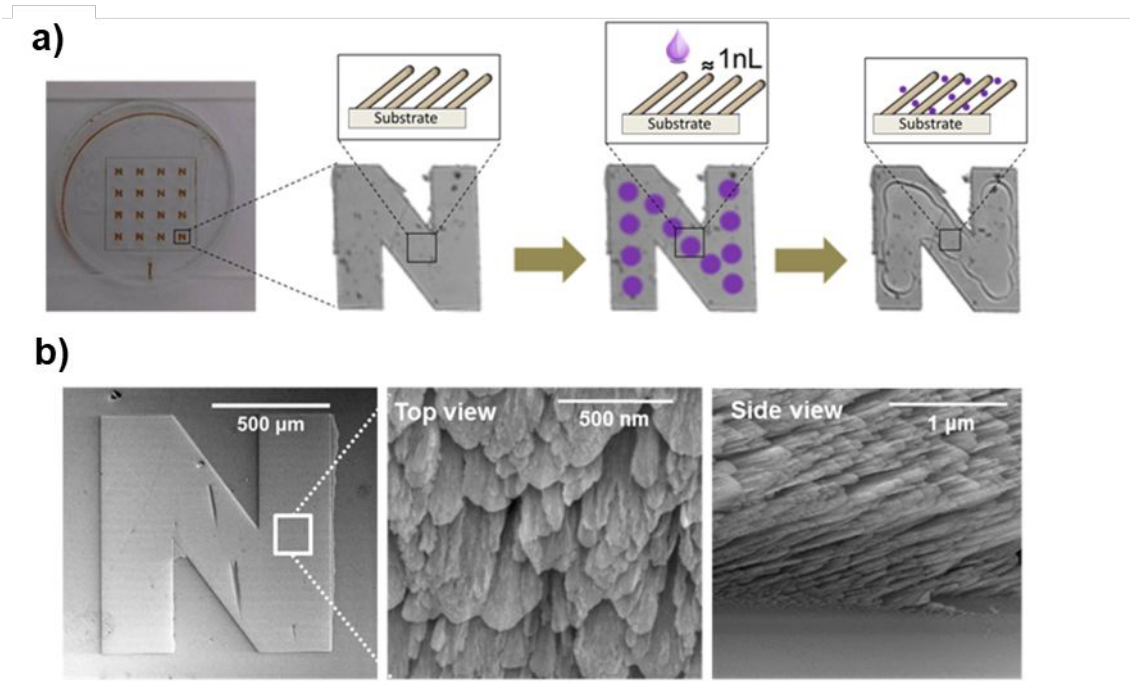

Fig. 4 a) Schematic of locations for controlled piezoelectric printing of nano-liter-sized volumes of TiO_2NP solution within a Al_2O_3-Si-SCTF `N'-shape. C) Top-view and high-resolution cross-section electron microscope images of the Al_2O_3-Si-SCTF.

2.6. Sensing Experiments under Flow Conditions

Rotation scan characterization by ACOM is needed to find the initial properties of Al_2O_3-Si-SCTF (H, Θ, Φ, f_{Si}, f_{water}, q_z, $split_{xy}$) in water ambient. First, to obtain to the baseline before nanoparticle injection, a single I_D was dynamically measured over the entire SCTF area with fixed α_p and α_c while water was flowing inside the microfluidic channel. The microfluidic channel filled with water was placed in the ACOM with fixed polarizer and compensator azimuth settings (α_p and α_c) relative to the fix analyzer azimuth, such that the SCTF surface brightened while the glass surface darkened (Figure 2c-1) (Table 2). Then, the averaged I_D was recorded as a single data point over the entire SCTF surface and throughout the experiment. Once the averaged change in the normalized intensity data ($\Delta I_{D(t=i)} = \frac{I_{D(t=i)} - I_{D(t=0)}}{I_{D(t=0)}}$) over the entire SCTF pixel points was less than 0.001/hr, rotation scan characterization was performed. Properties of the Al_2O_3-Si-SCTF (H, Θ, Φ, f_{Si}, f_{water}, q_z, $split_{xy}$) were estimated by best matching the ACOM recorded intensity data using a proper GE model. The dynamic measurement was then again set to start by fixing α_c and α_p to the previous values (Table 2). After several minutes of water introduction into the

microfluidic channel, 50 ppm TiO_2NP in water solution was introduced into the channel at a flow rate of either 15 µl/min or 50 µl/min. Changes in the single normalized intensity data ($\Delta I_{D(t)}$) over the duration of the experiments were instantly recorded while TiO_2NP solution was flowing inside the channel. TiO_2NP was introduced into the channel for 270 min and 81 min for the experiments at a flow rate of 15 µl/min (Test 2-1 and Test 2-2) and 50 µl/min (Test 2-3 and Test 2-4), respectively, to ensure that an equal mass of TiO_2NPs was introduced into the channel in the two experiments. After dynamic measurement was completed, another set of rotation scans was conducted to find the areal mass density distribution of TiO_2NPs on the SCTF surface for each pixel point.

Using the AB-EMA model, changes of I_D over time for a fixed value of α_p and α_c were best matched to the ACOM intensity data. The deposition of TiO_2NP over the entire SCTF surface with known SCTF properties (H, Θ, Φ, f_{Si}, f_{water}, q_z, $split_{xy}$) was calculated using the single intensity data over time. However, during the rotation scan ($\alpha_c=3\alpha_p$), 360 different intensity data were measured for each pixel point by ACOM. The AB-EMA model was used on each pixel point to find f_{TiO_2}, which best matched the 360 intensity data points measured by ACOM (Figure 2, and 3).

2.7. Computational Fluid Dynamic Modeling of Flow in SCTF

The computational fluid dynamic (CFD) package in COMSOL Multiphysics software (version 4.4) was used to simulate the flow field between SCTF posts at flow rates of 15 µl/min and 50 µl/min. In this simulation, the Navier-Stokes equation was coupled with the continuity equation to obtain a flow velocity field. A constant flow rate boundary condition of 15 µl/min or 50 µl/min was applied at the inlet boundary, and a zero pressure boundary condition was applied at the outlet boundary. An extremely fine mesh was used to discretize the domain. A fully coupled direct solver was selected for numerical calculation.

3. Results and Discussion

3.1. TiO_2NP and Al_2O_3-Si-SCTF Surface Characterization

The zeta potentials of the 1500 ppm and 50 ppm TiO_2NP in water solution were -26.9±2.5 mV and -16.5±3.4 mV, respectively. Figure 5 depicts that hydrodynamic diameter distributions of 1500 ppm and 50 ppm TiO_2NP in water were between 1 and 50 nm. Because the average space between individual columns of the Al_2O_3-Si-SCTF was about 50 nm (Figure 4b), we expected that majority of TiO_2NPs, particularly those with smaller sizes, can penetrate and potentially deposit within the porous structures.

The structural parameters of Al_2O_3-Si-SCTF (H, Θ, Φ, q_z, $split_{xy}$, f_{Si}, and $f_{ambient}$) prior to TiO_2NP exposure were estimated using the AB-EMA model (Figure 3), as provided in Tables 1 and 2 for air and water ambient conditions, respectively. The best match modeled parameters generally agreed with the nominal growth parameters. Particularly, the SCTF thickness (H) was in the range of 430 to 511 nm for all the experiments, which is consistent with the intended thickness of 500 nm. The slanting angle of all experiments ranged from 51 to 67°, which is also consistent with the intended slanting angle of 60°. Both parameters are generally in agreement with the SEM image analysis (Figure 4b). The small variation among experiments can be attributed to small variations of experimental conditions across the deposited area. The model calculated azimuth orientation of the column slanting plane relative to the linear polarization direction of the fixed analyzer azimuth (Φ) was also consistent with the experimental slanting direction during the imaging experiment. Φ was set at 0° for Test 1-1 and Test 1-3, and at 45° for Test 1-2. We note that the structural parameters of Al_2O_3-Si-SCTF estimated by the best-matched model were not sensitive to the choice of Φ.

Although SCTFs with 500 nm thicknesses were used in this study, this method is applicable for any heights of SCTFs, as long as the SCTF posts are slanted, the hydrodynamic size of nanoparticles is smaller than the height of SCTFs and the spacing between SCTFs posts. The size of SCTFs used in this study is in the same range of surface roughness of natural sand grains and glass beads. For example, Rasmuson et al.[37] represented environmental surfaces by creating roughness on glass. They have reported that for untreated, NaOH-treated, and HF-treated glass slides, the root-mean square surface roughness measured by AFM were <1 nm, 38 nm, and 546 nm, respectively. Shen et al.[38] showed that the AFM measured maximum and the root-mean square surface roughness of 40/60 mesh quartz sand were 2418 nm and 355 nm[38,39].

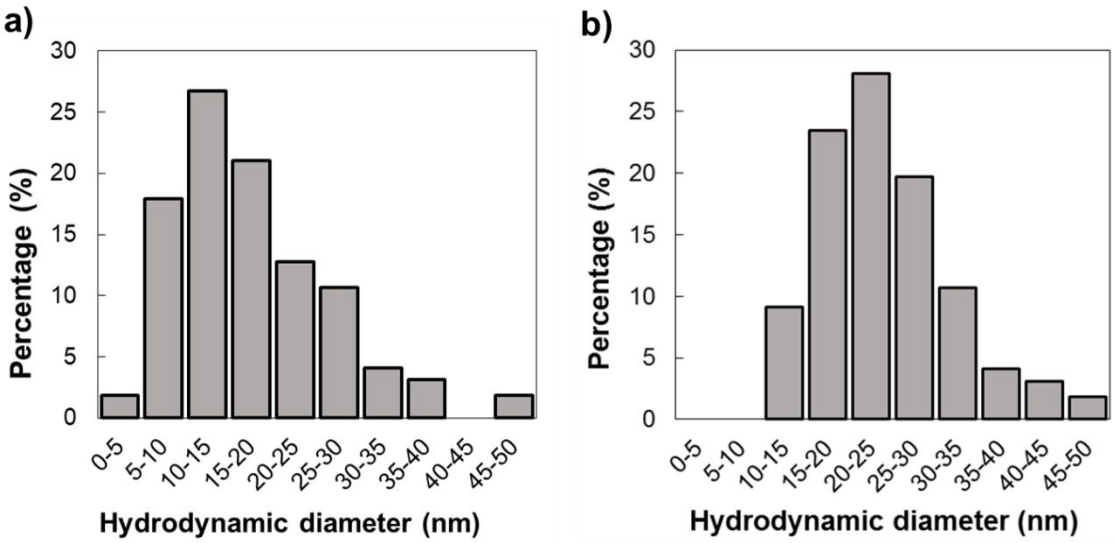

Fig. 5 Hydrodynamic diameter of TiO_2NP in a) 1500 ppm and b) 50 ppm water solution.

Table 1 Structural and optical parameters of Al_2O_3-Si-SCTF in air ambient on glass substrate under ACOM instrumentation. The error bars correspond to the 90% confidence interval.

Parameters	Test 1-1	Test 1-2	Test 1-3
H [nm]	504±33	430±17	447±17
Θ[°]	62±2	67±1	66±1
Φ[°]	-0.3±0.2	45.6±0.3	-0.8±0.2
q_z	0.17±0.01	0.17±0.02	0.17±0.03
$split_{xy}$	0.37±0.02	0.38±0.08	0.41±0.04
f_{Si} [%]	25±2	27±2	27±2
f_{air} [%]	75±2	73±2	73±2
Total np mass ACOM $mMass_{TiO2NP}$ [ng]	21±9	15±5	63±5
Total np mass Print $eMass_{TiO2NP}$ [ng]	12±1	24±2	72±1

Table 2 Structural and optical parameters of Al_2O_3-Si-SCTF in water ambient inside the microfluidic channel under ACOM instrumentation. The error bars correspond to the 90% confidence interval.

Parameters	Test 2-1 Flow rate= 15 [µl/min]	Test 2-2 Flow rate= 15 [µl/min]	Test 2-3 Flow rate= 50 [µl/min]	Test 2-4 Flow rate= 50 [µl/min]
H [nm]	494±9	478±5	492±10	511±7
Θ[°]	51±1	54±1	51±1	54±1
Φ[°]	136±2	114±5	123±3	122±3
q_z	0.21±0.01	0.16±0.02	0.20±0.01	0.16±0.01
$split_{xy}$	0.46±0.02	0.42±0.05	0.45±0.01	0.41±0.05
f_{Si} [%]	33±2	34±1	34±1	31±1
f_{water} [%]	67±2	66±1	66±1	69±1
α_p [°]	29	29	30	29
α_c [°]	87	87	90	87

3.2. Sensing TiO_2NP in Air Ambient

Figure 6a presents typical individual ACOM images of `N'-patterned Al_2O_3-Si-SCTF on glass substrate after nanoparticle exposure under a fixed α_p and fixed α_c. Based on the GE data analysis

approach described above, f_{TiO_2} was estimated for every pixel area A (7 µm × 7 µm). The mass of nanoparticle per pixel, $Mass_{TiO_2NP}$, was estimated as (Figure 6b):

$$Mass_{TiO_2NP} = f_{TiO_2} \times H \times \rho_{TiO_2} \times A. \quad (5)$$

The corresponding number quantities of nanoparticles per pixel (noted on the color bar) was also estimated for each pixel by assuming an average mass of approximately 11 attograms per nanoparticle with 17.8 nm in diameter.

Mass distribution images (Figure 6b) clearly delineate the areas where TiO_2NPs were deposited, with non-uniform distributions of TiO_2NP mass in the SCTF area. For the experiments with more TiO_2NP printed, the ACOM images showed overall higher mass of TiO_2NP in the printed area. Test 1-3, the experiment with the highest exposure to nanoparticles, revealed the largest accumulation of mass and more spread of nanoparticles during the evaporation process. A clearly visible coffee stain effect emerged with increasing TiO_2NP exposure, revealing a higher concentration of nanoparticles close to the edge of droplets due to the water evaporation process. The average value of the parameter uncertainty for mass, δMass, and accordingly, δnumber, over the observed image area were also provided (Figure 6) for all three tests. The total masses of nanoparticles estimated by integrating the ACOM mass distribution images were 21 ng, 15 ng, and 63 ng for Test 1-1, Test 1-2, and Test 1-3, respectively, which compared reasonably with the total mass of printed nanoparticles of 12 ng, 24 ng, and 72 ng, respectively (Table 1, Figure 6d). In all tests, the ACOM estimated mass is within the margin of error of the total nanoplotted mass. Figure 6d illustrates that this technique is capable to detect trivial amount of TiO_2NP mass reasonably well.

We note here that the structural and optical parameters were assumed to be constant over the image area in our analysis. However, local variations in SCTF properties as well as local defects in SCTF coverage always exist, which contributed to the observed deviations between the total printed and total measured mass values, as well as uncertainties of estimated mass (δMass) per pixel. For mass distribution images (Figure 6 a, b), spurious red pixels were observed along some boundaries of the `N'-shape SCTF. This artifact can be attributed to the GE analysis errors caused by boundary pixels that partially contain bare glass and SCTF surfaces. For these boundary pixels, the structural and optical parameters for Al_2O_3-Si-SCTF that were used in the AB-EMA

model did not reflect the actual properties of those pixel points. Therefore, the mass distribution of TiO_2NP on the Al_2O_3-Si-SCTF surface is artificial along these edges. Because the deposition of the TiO_2NP solution was performed along the center line of the `N'-shape Al_2O_3-Si-SCTF area, the masses calculated based on GE analysis around the edge of the SCTF areas are disregarded in our further analysis. For Test 1-2 and 1-3 with a higher mass load, we also note the possibility that small portions of the nanoparticle solution may have flown outside the SCTF areas prior to solvent evaporation, thereby transporting small fractions of nanoparticles onto the optically isotropic glass surface. Nanoparticles residing in the bare glass surface areas are undetectable to ACOM, which partially explains the fact that the model slightly underestimated the mass (Figure 6d) for tests 1-2 and 1-3.

The demonstrated capability of sensing nanoparticles on a highly ordered columnar nanostructured surface in air ambient is unprecedented. We were able to detect a few picograms of nanoparticles (17.8 nm in diameter) within a sample surface area of approximately 7 μm×7 μm without the help of any labeling technique. In addition to mass distribution images, we have demonstrated a reasonably accurate quantitative capability of the technique (Figure 6d). The sensing capability demonstrated here is better than the currently prevalent particle sensing instrumentation, for example, QCM-D. Although QCM-D can dynamically measure the overall mass of nanoparticles attached on its surface[40,41], it cannot quantify the distribution of the attached nanoparticles on the sensor surface.

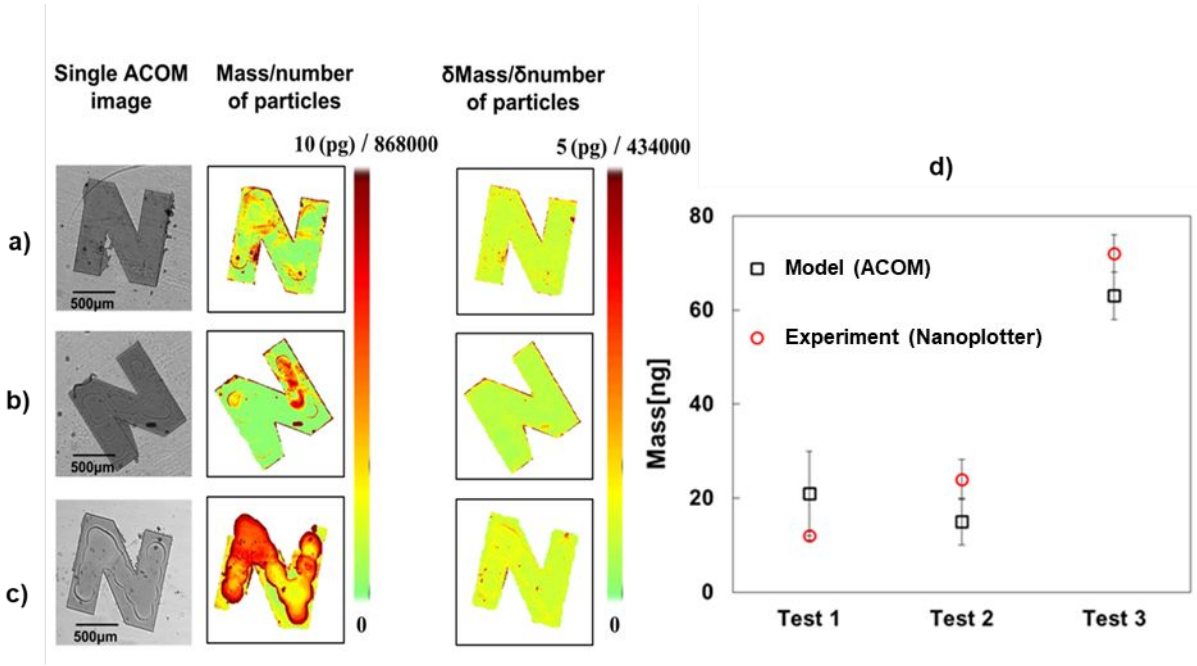

Fig. 6 Images in rows (a), (b), and (c) pertain to Test 1-1, Test 1-2, and Test 1-3, respectively. Left column: Individual ACOM images of patterned Al_2O_3-Si-SCTF on glass substrate after nanoparticle exposure; Middle column: Images of nanoparticle mass distribution. The scale bars also depict the numerical quantities for nanoparticle number distribution across the SCTF surface (see text); Third column: Images of numerical uncertainty of nanoparticle mass and number distributions. d) Comparison of total integrated mass of TiO_2NP printed by nanoplotter (`Experiment') and total integrated mass obtained from the ACOM image analysis (`Model'). The error bars correspond to the 90% confidence interval. The ellipsometric model includes the glass slide and the AB-EMA model layer for the anisotropic Si-SCTF surface. (Field of view: 3.73 mm×3.73 mm, presented area: 1.74 mm×1.74 mm, resolution: 7 µm×7 µm sample surface area imaged per pixel; λ=633 nm).

3.3. Sensing TiO_2NPs under Flow Condition

Based on the intensity change captured by ACOM, the AB-EMA model can be used to estimate the areal mass density of TiO_2NP attached to the surface of Al_2O_3-Si-SCTF (Γ_{TiO_2}) as TiO_2NP was introduced into the microfluidic channel. Figure 7a and b showed an increase in Γ_{TiO_2} over time while TiO_2NP solution was flowing inside the channel. Note that the shaded areas in Figure 7 correspond to the ACOM detection limit, which was averaged as ±250 ng/cm^2 (2.5 fg/µm^2). In our previous publication[20], the detection limit for cetyltrimethylammonium bromide (CTAB) was determined as 1 fg/µm2. Because TiO_2NPs are larger than CTAB molecules, higher level of random depolarization and scattering will occur when light hits TiO_2NPs, which led to larger error bars for the ellipsometry measurement, and therefore, a higher detection limit. The accuracy of this technique depends on the calibration of SCTF surface prior to nanoparticles deposition,

which finds proper structural and optical properties of SCTF. Here accuracy was on the same order of magnitude to detection limit, because SCTF surface was calibrated correctly.

Repeated experiments were conducted at a lower flow rate of 15 µl/min (Figure 7a) and a higher flow rate of 50 µl/min (Figure 7b). Here, repeated experiments were conducted using two different microfluidic channels with SCTFs embedded. Although the Al_2O_3-Si-SCTF surface in each channel possesses the same average properties, nanoscale non-uniformities are expected for each individual surface. Because ACOM is very sensitive to any nanoscale attachment, it is expected that two repeated experiments could reproduce similar trends of mass increase but not the exact same amount over time. It should be noted that, the sudden increase and decrease of the areal mass density of attached TiO_2NPs for Test 2-2 (Figure 7a) at the initial stage of the experiment was due to the entrance of a bubble into the microfluidic channel, which interfered the intensity measurement. After that, the measurement was back to normal and showed similar trend of TiO_2NP attachment as the parallel experiment (Test 2-1).

As shown in Figure 7, Γ_{TiO_2} gradually increased for all the experiments while TiO_2NP solution was introduced into the microfluidic channels. After the same amount of TiO_2NP mass (i.e., 203 µg) was introduced, Γ_{TiO_2} reached 1837±301 ng/cm^2 and 1890±168 ng/cm^2 for lower flow rate experiments (i.e., tests 2-1 and 2-2) and 1200±244 ng/cm^2 and 920±284 ng/cm^2 for higher flow rate experiments (i.e., tests 2-3 and 2-4). The repeated experiments under both flow rates were in close agreement regarding the total amount of TiO_2NP mass attached on the SCTFs. The slopes of the mass increase were also consistent between repeated experiments under both flow rates, indicating the reproducibility of the technique. More mass of TiO_2NPs were attached to the SCTF surface per mass of TiO_2NP introduced into the channel under the lower flow rate than the higher flow rate. This is depicted by the slope of the curves in Figure 7 and is due to the longer residence time of TiO_2NPs in the microfluidic device corresponding to the lower flow rate. The average attached mass rate, defined by the ratio of Γ_{TiO_2} to the injection time, was 6.9 ng/cm^{2}min for the lower flow rate experiments (Test 2-1 and Test 2-2) and 14.3 ng/cm^{2}min for the higher flow rate experiments (Test 2-3 and Test 2-4).

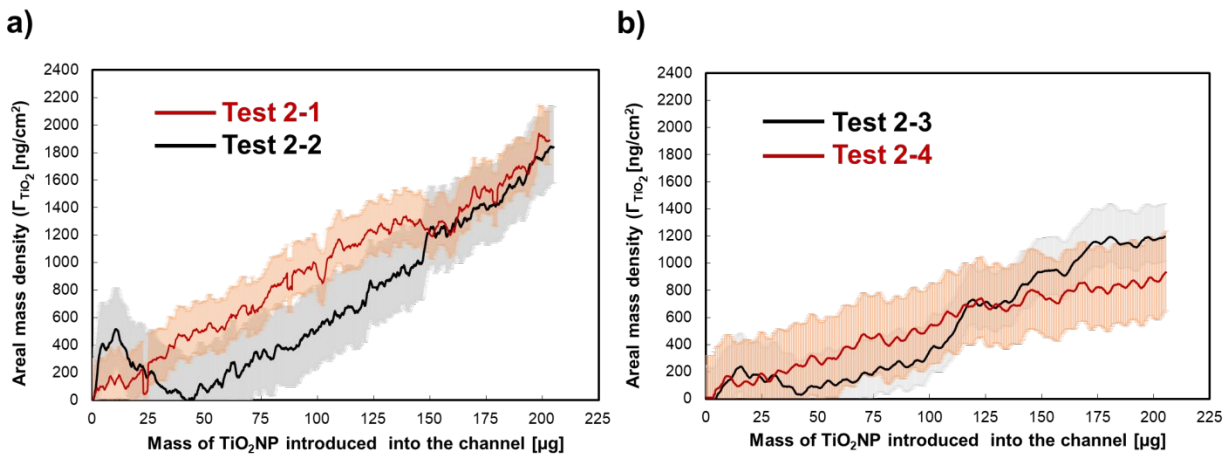

Fig. 7 The areal mass density of the attached TiO_2NP on the Al_2O_3-Si-SCTF surface for the flow rates of a)15 µl/min and b) 50 µl/min of 50 ppm TiO_2NPs solution.

Figure 8a shows representative intensity images in the location adjacent to the channel inlet at a fixed α_p and fixed α_c setting (depicted in Table 2) before introducing TiO_2NP solution into the microfluidic channel. Figure 8b depicts the corresponding distribution of attached TiO_2NP on the Al_2O_3-Si-SCTF surface at the end of the experiment, at each individual pixel point, with color scale bars in terms of mass density (Γ_{TiO_2}), mass of TiO_2NP per pixel ($Mass_{TiO_2}$), and the number of TiO_2NP per pixel (N_{TiO_2}). Here, $Mass_{TiO_2}$ was calculated by multiplying Γ_{TiO_2} with the area of each individual pixel point. N_{TiO_2} was also calculated from the mass of an individual TiO_2NP assuming an average hydrodynamic diameter of 24 nm (Figure 5b). Figure 8c represents the example comparison between the ACOM experimental intensity measurement and AB-EMA best-matched I_D scaled by the measured maximum I_D data (SI_D) for each test at a selected individual pixel. The R-squared values for all best-matched single pixel points were higher than 0.9.

Distributions of TiO_2NP were not uniform on the surface of Al_2O_3-Si-SCTF for each individual test. Some pixel points showed more particles while others showed less or no TiO_2NP. The spatial distribution of TiO_2NP on the Al_2O_3-Si-SCTF surface was not expected to be the same between repeated experiments (Test 2-1 and 2-2; Test 2-3 and 2-4) due to the nanoscale non-uniformities on the surface of Al_2O_3-Si-SCTF as explained earlier and shown in Figure 8a. However, the overall attachments revealed by integrating the particle mass on the area were

consistent between each repeated experiment. The averaged Γ_{TiO_2} for the entire area of Al_2O_3-Si-SCTF based on the Γ_{TiO_2} distribution (Figure 8b) were 1183 ng/cm^2, 1778 ng/cm^2, 1293 ng/cm^2, and 968 ng/cm^2 for Test 2-1, Test 2-2, Test 2-3, and Test 2-4, respectively. Most importantly, the averaged Γ_{TiO_2} estimated based on Figure 8b had good agreement with the dynamic measurement of Γ_{TiO_2}, as depicted in Figure 9. Two approaches estimated a similar average mass density of TiO_2NP at the end of the experiments, which further demonstrates the ability of this sensing technique to quantitatively determine the areal mass density of nanoparticles on a SCTF surface (Figure 9).

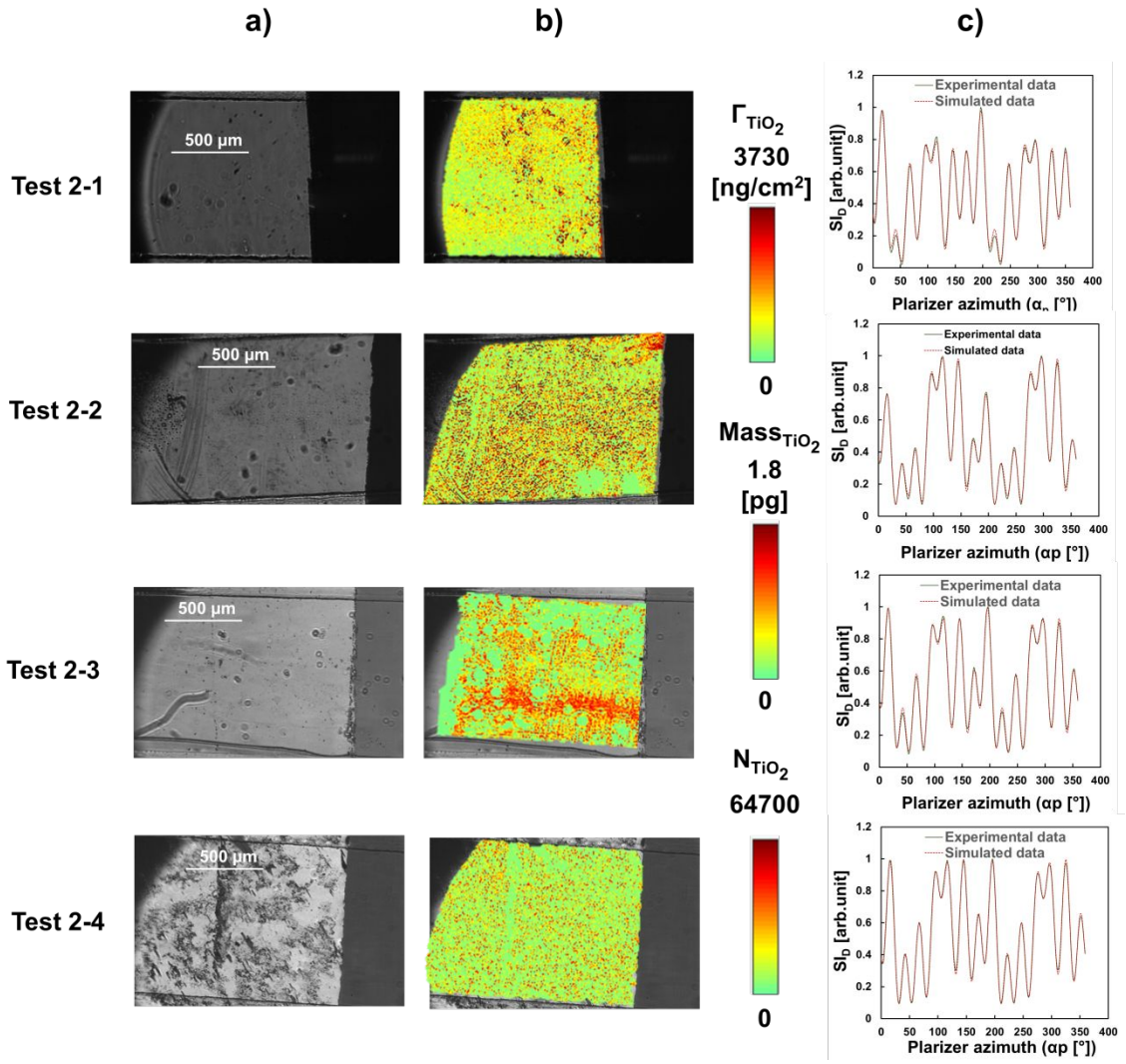

Fig. 8 a) ACOM intensity images at selected polarizer azimuth settings (refer to table 2). b) Distribution of areal mass density, mass, and number of attached TiO_2NP on Al_2O_3-Si-SCTF surface (ΓTiO_2) for each individual pixel. c) ACOM

Measured and AB-EMA best-matched scaled intensity data (SI_D) using ACOM and AB-EMA model respectively for one pixel point (R^2=0.99).

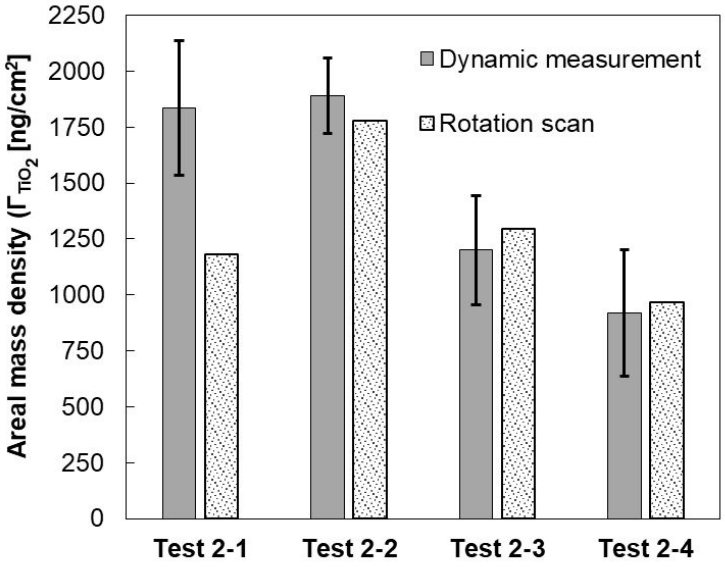

Fig. 9 Areal mass density of attached TiO_2NP on SCTF surface inside microfluidic channel calculated based on dynamic measurement (fixed α_p and α_c), and the rotation scan data (α_c=3α_p).

Comparing experiments under different flow rates, more TiO_2NPs were attached under the lower flow rate, although the attached mass rate was higher for the higher flow rates. Figure 10 presents the CFD simulated flow velocity distribution inside SCTF under flow rates of 15 and 50 µl/min. The Reynolds numbers for flow in between SCTF posts and at a SCTF scale were estimated as 4.33×10^{-5} and 1.5×10^{-3} for flow rates of 15 and 50 µl/min, respectively, considering an SCTF characteristic length of 870 nm and the average velocity between two SCTF posts. As both flow conditions are laminar, TiO_2NP nanoparticles need to come across the flow streamlines to approach the surface of SCTF. For nanoparticles measuring 24 nm in diameter, diffusion is the dominating mechanism for attachment. Nanoparticles would easier come across flow streamline under the higher flow rate where a sharper velocity gradient exists adjacent to the SCTF surface. Although the surface charges of Al_2O_3-Si-SCTFs were not measured in our study, Gu et al.[42] calculated a positive charge of 25 mV for the thin ALD layer of alumina on a silicon wafer at pH 7 in 1 mM KCl solution, which is close to our condition. Once nanoparticles diffuse across the streamlines, a favorable attachment is expected to occur between negatively charged TiO_2NP

and positively charged Al_2O_3-Si-SCTF based on DLVO interaction theory[43]. Therefore, a higher attached mass rate under a higher flow rate is expected. The lower flow rate, however, allows longer residence time of nanoparticles inside SCTFs, so eventually more nanoparticles can diffuse across the flow streamlines and get closer to the SCTF surface. Hence, a higher retention amount of TiO_2NP corresponds to the same mass of TiO_2NP introduced into the microfluidic channel under a lower flow rate than a higher flow rate.

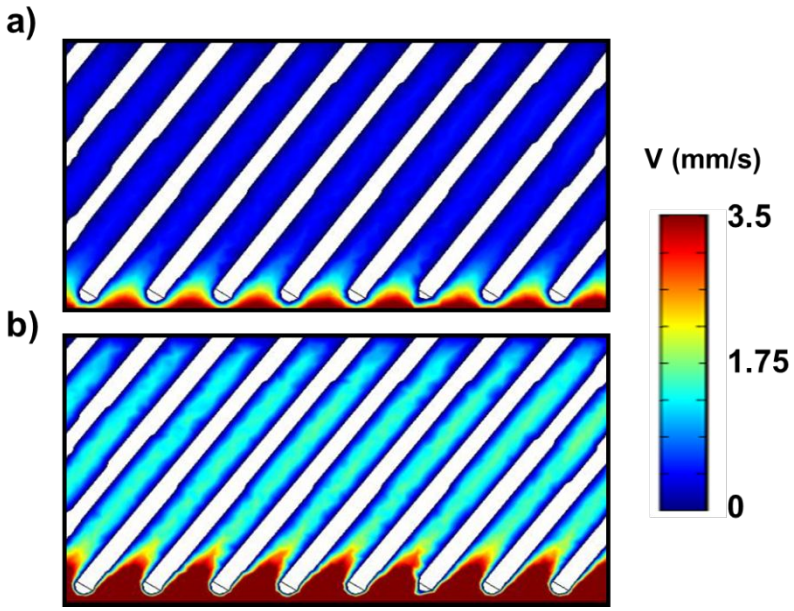

Fig. 10 Velocity distributions between SCTF posts for the flowrates of a) 15 µl/min, and b) 50 µl/min.

4- Conclusions

In summary, we demonstrated an innovative technique to visualize and quantify the deposition of non-labeled TiO_2NP with a diameter smaller than 50 nm on model Al_2O_3-Si-SCTF rough surfaces in air and under flow conditions using ACOM. We first demonstrated the capability of using ACOM and the appropriate optical model to measure the distribution of TiO_2NP on the SCTF rough surface by dropping a known amount of TiO_2NP onto the surface. We found reasonable agreement between the ACOM measured and dropped mass of TiO_2NPs. Detection of a few picograms of nanoparticle mass by an individual pixel of 7×7 µm^2 was presented. We

then applied the same technique to measure and visualize the attachment of label-free TiO_2NP on an engineered 500-nm-thick Al_2O_3-Si-SCTF surface inside glass microfluidic channels at two different flow rates. We demonstrated the ability to instantly measure the deposition of TiO_2NP on these surfaces during the introduction of TiO_2NP into the microfluidic channel. During the introduction of 203 μg of TiO_2NP, the averaged attached TiO_2NP mass density on the Al_2O_3-Si-SCTF surface was 1.6-fold higher at a flow rate of 15 μl/min compared to 50 μl/min. However, the deposition rate was higher under a higher flow rate, which was expected and reasonable based on flow simulation. We were able to visualize the distribution of the attached TiO_2NP on the Al_2O_3-Si-SCTF surface at the end of the TiO_2NP solution introduction into the microfluidic channel. Although the detailed distribution map of TiO_2NP was different between experiments due to nanoscale non-uniformities, the averaged mass density estimated by integrating the distribution map was in close agreement with the estimation from dynamic measurements and between repeated experiments.

By implementing the ACOM instrument with the proper optical model, we were able to visualize and quantify the distribution of TiO_2NP on the SCTF surface under both static and flow conditions. This technique can be applied to any type of nanoparticles with hydrodynamic sizes smaller than the height and spaces between SCTF posts, given the optical properties of nanoparticles (i.e. refractive index, extinction coefficient) are known. Technically it is possible to manufacture SCTF with different dimensions; therefore, this method can be applicable to a wide range of nanoparticles or the mixture of nanoparticles, although it cannot differentiate between different types of nanoparticles. As proof-of-concept, experiments in this study was conducted with simple water chemistry. The method is applicable to more environmentally relevant water condition with various dissolved ions present. If water contains solutes that may attach to the surface of SCTF, e.g. natural organic matter, the technique is also applicable but requires an additional calibration step to quantify the attachment of the additional solutes on SCTF surfaces. In addition, by manipulating the physical and chemical properties of SCTF surfaces, for example covering the part of the SCTF surfaces with natural organic matters (NOM) using lithography technique, this technique will provide an innovative avenue to investigate interaction of label-free ENPs with rough surfaces of various properties.

Conflicts of interest

Authors declare no conflict of interest.

Acknowledgment

Support for this research was provided in part by funds from the Center for Nanohybrid Functional Materials (NSF-EPS-10004094), NSF awards CBET- 1133528, CBET- 1521428, and the American Chemical Society Petroleum Research Funds PRF # 59374-ND5. We thank Thomas Wegener and Thomas Gehring form Gesim Co. for their help with the project. The research was performed in part in the Nebraska Nanoscale Facility: National Nanotechnology Coordinated Infrastructure and the Nebraska Center for Materials and Nanoscience, which are supported by the National Science Foundation under Award ECCS: 1542182, and the Nebraska Research Initiative.

References

(1) Robichaud, C. O.; Uyar, A. E.; Darby, M. R.; Zucker, L. G.; Wiesner, M. R. Estimates of upper bounds and trends in nano-TiO2 production as a basis for exposure assessment. **2009**, 4227–4233.

(2) Keller, A. A.; Lazareva, A. Predicted releases of engineered nanomaterials: from global to regional to local. *Environ. Sci. Technol. Lett.* **2013**, *1* (1), 65–70.

(3) Mansfield, C. M.; Alloy, M. M.; Hamilton, J.; Verbeck, G. F.; Newton, K.; Klaine, S. J.; Roberts, A. P. Photo-induced toxicity of titanium dioxide nanoparticles to Daphnia magna under natural sunlight. *Chemosphere* **2015**, *120*, 206–210.

(4) Chen, G.; Liu, X.; Chunming, S. Transport and Retention of TiO2 Rutile Nanoparticles in Saturated Porous Media under Low-Ionic-Strength Conditions: Measurements and Mechanisms. *Langmuir* **2011**, *27* (9), 5393–5402.

(5) Chen, G.; Liu, X.; Su, C. Distinct Effects of Humic Acid on Transport and Retention of TiO2 Rutile Nanoparticles in Saturated Sand Columns. *Env. Sci Technol* **2012**, *46*, 7142–7150.

(6) Choy, C. C.; Wazne, M.; Meng, X. G. Application of an empirical transport model to simulate retention of nanocrystalline titanium dioxide in sand columns. *Chemosphere* **2008**, *71* (9), 1794–1801.

(7) Joo, S. H.; Al-Abed, S. R.; Luxton, T. Influence of Carboxymethyl Cellulose for the Transport of Titanium Dioxide Nanoparticles in Clean Silica and Mineral-Coated Sands. *Environ. Sci. Technol.* **2009**, *43* (13), 4954–4959.

(8) Cornelis, G.; Hund-Rinke, K.; Kuhlbusch, T.; Van den Brink, N.; Nickel, C. Fate and bioavailability of engineered nanoparticles in soils: a review (2014): *Crit. Rev. Environ. Sci. Technol.* **2014**, *44*, 2720–2764.

(9) Cornelis, G.; Pang, L.; Doolette, C.; Kirby, J. K.; McLaughlin, M. J. Transport of silver nanoparticles

in saturated columns of natural soils. *Sci. Total Environ.* **2013**, *436–464*, 120–130.

(10) Cornelis, G.; Doolette, C.; Thomas, M.; McLaughlin, M. J.; Kirby, J. K.; Beak, D. G.; Chittleborough, D. Retention and dissolution of engineered silver nanoparticles in natural soils. *Soil Sci. Soc. Am. J.* **2012**, *76*, 891–902.

(11) Thio, B. J. R.; Zhou, D.; Keller, A. A. Influence of natural organic matter on the aggregation and deposition of titanium dioxide nanoparticles. *J. Hazard. Mater.* **2011**, *189* (1–2), 556–563.

(12) Kananizadeh, N.; Rice, C.; Lee, J.; Rodenhausen, K. B.; Sekora, D.; Schubert, M.; Schubert, E.; Bartelt-Hunt, S.; Li, Y. Combined quartz crystal microbalance with dissipation (QCM-D) and generalized ellipsometry (GE) to characterize the deposition of titanium dioxide nanoparticles on model rough surfaces. *J. Hazard. Mater.* **2017**, *322*.

(13) Fatisson, J.; Domingos, R. F.; Wilkinson, K. J.; Tufenkji, N. Deposition of TiO2 nanoparticles onto silica measured using a Quartz Crystal Microbalance with Dissipation monitoring. *Langmuir* **2009**, *25* (11), 6062–6069.

(14) Guzman, K. A. D.; Finnegan, M. P.; Banfield, J. F. Influence of surface potential on aggregation and transport of titania nanoparticles. *Environ. Sci. Technol.* **2006**, *40* (24), 7688–7693.

(15) Kusaka, Y.; Duval, J. F. L.; Adachi, Y. Morphology and Breaking of Latex Particle Deposits at a Cylindrical Collector in a Microfluidic Chamber. *Env. Sci Technol* **2010**, *44*, 9413–9418.

(16) de Saint Vincent, M. R.; Abkarian, M.; Tabuteau, H. Dynamics of colloid accumulation under flow over porous obstacles. *Soft Matter* **2016**, *12* (4), 1041–1050.

(17) Seymour, M. B.; Chen, G.; Su, C.; Li, Y. Transport and Retention of Colloids in Porous Media: Does Shape Really Matter? *Environ. Sci. Technol.* **2013**, *47* (15), 8391–8398.

(18) May, R.; Akbariyeh, S.; Li, Y. S. Pore-Scale investigation of nanoparticle transport in saturated porous media using laser scanning cytometry. *Environ. Sci. Technol.* **2012**, *46* (18), 9980–9986.

(19) Chen, C.; T.Waller; Walker, S. L. Visualization of transport and fate of nano and micro-scale particles in porous media: modeling coupled effects of ionic strength and size. *Environ. Sci. Nano* **2017**, *4*, 1025–1036.

(20) Peev, D.; Hofmann, T.; Kananizadeh, N.; Beeram, S.; Rodriguez, E.; Wimer, S.; Rodenhausen, B.; Herzinger, C. M.; Kasputis, T.; Pfaunmiller, E.; et al. Anisotropic contrast optical microscope. *Rev. Sci. Instrum.* **2016**, *87* (11), 113701.

(21) Fujiwara, H. *Spectroscopic Ellipsometry*; John Wiley & Sons: New York, 2007.

(22) Schubert, M.; Rheinlander, B.; Woollam, J. A.; Johs, B.; Herzinger, C. M. Extension of rotating-analyzer ellipsometry to generalized ellipsometry: Determination of the dielectric function tensor from uniaxial TiO2. *J. Opt. Soc. Am. a-Optics Image Sci. Vis.* **1996**, *13* (4), 875–883.

(23) Kananizadeh, N.; Rice, C.; Lee, J.; Rodenhausen, K. B.; Sekora, D.; Schubert, M.; Schubert, E.; Bartelt-Hunt, S.; Li, Y. Combined quartz crystal microbalance with dissipation (QCM-D) and generalized ellipsometry (GE) to characterize the deposition of titanium dioxide nanoparticles on model rough surfaces. *J. Hazard. Mater.* **2017**, *322*, 118–128.

(24) Rodenhausen, K. B.; Schmidt, D.; Rice, C.; Hofmann, T.; Schubert, E.; Schubert, M. Detection of organic attachment onto highly ordered three-dimensional nanostructure thin films by generalized ellipsometry and quartz crystal microbalance with dissipation techniques. In *Ellipsometry of Functional Organic Surfaces and Films*; Eichhorn, K., Ed.; Springer, Berlin, 2013.

(25) Schmidt, D.; Schubert, E.; Schubert, M. Generalized Ellipsometry Characterization of Sculptured Thin Films Made by Glancing Angle Deposition. In *Ellipsometry at the Nanoscale*; Losurdo, M., Hingerl, K., Eds.; Springer, 2013; pp 341–410.

(26) Liang, D.; Schmidt, D.; Wang, H.; Schubert, E.; Schubert, M. Generalized ellipsometry effective medium approximation analysis approach for porous slanted columnar thin films infiltrated with polymer. *Appl. Phys. Lett.* **2013**, *103*, 11906-1-11906–5.

(27) Scubert, M. *Handbook of ellipsometry*; Tompkins, H., Irene, E. A., Eds.; William Andrew, 2005.

(28) Schmidt, D.; Schubert, E.; Schubert, M. Optical properties of cobalt slanted columnar thin films passivated by atomic layer deposition. *Appl. Phys. Lett.* **2012**, *100*, 011912.
(29) Hawkeye, M. M.; J., B. M. Glancing angle deposition: fabrication, properties, and applications of micro-and nanostructured thin films. *J. Vac. Sci. Technol.* **2007**, *A 25.5*, 1317–1335.
(30) Liu, X.; Chen, G.; Su, C. Influence of Collector Surface Composition and Water Chemistry on the Deposition of Cerium Dioxide Nanoparticles: QCM-D and Column Experiment Approaches. *Environ. Sci. Technol.* **2012**, *46* (12), 6681–6688.
(31) Olsson, A. L. J.; Quevedo, I. R.; He, D.; Basnet, M.; Tufenkji, N. Using the Quartz Crystal Microbalance with Dissipation Monitoring to Evaluate the Size of Nanoparticles Deposited on Surfaces. *ACS Nano* **2013**, *7* (9), 7833–7843.
(32) Schmidt, D.; Schubert, M. Anisotropic Bruggeman effective medium approaches for slanted columnar thin films. *J. Appl. Phys.* **2013**, *114* (8), 083510.
(33) E. D. Palik. *Handbook of Optical Constants of Solids*; Academic Press: New York, 1998.
(34) Rodenhausen, K. B.; Davis, R. S.; Sekora, D.; Liang, D.; Mock, A.; Neupane, R.; Schmidt, D.; Hofmann, T.; Schubert, E.; M. Schubert. The retention of liquid by columnar nanostructured surfaces during quartz crystal microbalance measurements and the effects of adsorption thereon. *J. Colloid Interface Sci.* **2015**, *455*, 226–235.
(35) Losurdo, M.; Hingerl, K. *Ellipsometry at the nanoscale*; Springer Science & Business Media, 2013.
(36) Kuzyk, M. C.; Dirk, C. W. *Characterization techniques and tabulations for organic nonlinear optical materials*; Marcel Dekker, Inc., 1998.
(37) Rasmuson, A.; Pazmino, E.; Assemi, S.; Johnson, W. P. Contribution of nano- to microscale roghness to heterogeneity: closing the gap between unfavorable and favorable colloid attachment conditions. *Env. Sci Technol* **2017**, *51*, 2151–2160.
(38) Shen, C. Y.; Li, B. G.; Wang, C.; Huang, Y. F.; Jin, Y. Surface roughness effect on deposition of nano- and micro-sized colloids in saturated columns at different solution ionic strengths. *Vadose Zo. J.* **2011**, *10* (3), 1071–1081.
(39) Torkzaban, S.; Bradfor, S. A. Critical role of surface roughness on colloid retention and release in the porous media. *Water Res.* **2016**, *88*, 274–284.
(40) Fatisson, J.; Ghoshal, S.; Tufenkji, N. Deposition of carboxymethylcellulose-coated zero-valent Iron nanoparticles onto silica: Roles of solution chemistry and organic molecules. *Langmuir* **2010**, *26* (15), 12832–12840.
(41) Thio, B. J. R.; Zhou, D.; Keller, A. A. Influence of natural organic matter on the aggregation and deposition of titanium dioxide nanoparticles. *J. Hazard. Mater.* **2011**, *189*, 556–563.
(42) Gu, D.; Yalcin, S.; Baumgart, H.; Qian, S.; Baysal, O.; Beskok, A. Electrophoretic Light Scattering for Surface Zeta Potential Measurement of ALD Metal Oxide Films. *ECS Trans.* **2010**, *33* (2), 37–41.
(43) Elimelech, M.; Gregory, J.; Jia, X.; Williams, R. A. *Particle deposition and aggregation: measurement, modeling and simulation*; Butterworth-Heinemann: Oxford, England, 1995.

Graphical Abstract

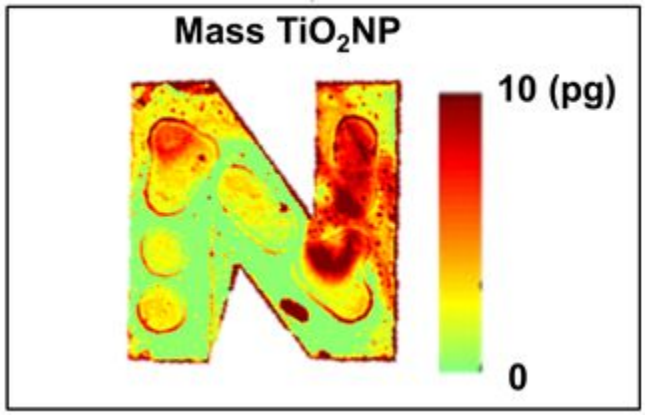

An innovative technique to quantify and visualize label-free titanium dioxide nanoparticles on model rough surfaces.